Nanoscale

PAPER

View Article Online
View Journal | View Issue

Cite this: *Nanoscale*, 2021, **13**, 16672

Tailorable multifunctionalities in ultrathin 2D Bi-based layered supercell structures†

Zihao He, [a] Xingyao Gao,[b] Di Zhang, [b] Ping Lu, [c] Xuejing Wang,[b] Matias Kalaswad,[a] Bethany X. Rutherford[b] and Haiyan Wang *[a,b]

Received 31st July 2021,
Accepted 22nd September 2021

DOI: 10.1039/d1nr04975e

rsc.li/nanoscale

Two-dimensional (2D) materials with robust ferromagnetic behavior have attracted great interest because of their potential applications in next-generation nanoelectronic devices. Aside from graphene and transition metal dichalcogenides, Bi-based layered oxide materials are a group of prospective candidates due to their superior room-temperature multiferroic response. Here, an ultrathin $Bi_3Fe_2Mn_2O_{10+\delta}$ layered supercell (BFMO322 LS) structure was deposited on an $LaAlO_3$ (LAO) (001) substrate using pulsed laser deposition. Microstructural analysis suggests that a layered supercell (LS) structure consisting of two-layer-thick Bi–O slabs and two-layer-thick Mn/Fe–O octahedra slabs was formed on top of the pseudo-perovskite interlayer (IL). A robust saturation magnetization value of 129 and 96 emu cm^{-3} is achieved in a 12.3 nm thick film in the in-plane (IP) and out-of-plane (OP) directions, respectively. The ferromagnetism, dielectric permittivity, and optical bandgap of the ultrathin BFMO films can be effectively tuned by thickness and morphology variation. In addition, the anisotropy of all ultrathin BFMO films switches from OP dominating to IP dominating as the thickness increases. This study demonstrates the ultrathin BFMO film with tunable multifunctionalities as a promising candidate for novel integrated spintronic devices.

Introduction

Motivated by the demonstration of graphene with astonishing properties,[1,2] the growing family of two-dimensional (2D) materials including transition metal dichalcogenides (TMDs),[3,4] Ruddlesden–Popper perovskites,[5,6] and 2D metal–organic frameworks[7,8] are rising as promising candidates for next-generation spintronics, optoelectronics, and nanoelectronics.[9–11] The recent discovery of magnetic ordering in 2D materials has attracted intense focus to explore magnetism in low-dimensional systems.[12,13] To address their practical device applications, high Curie temperatures (T_c) in 2D ferromagnetic materials are desired.

By integrating a ferromagnetic material with a ferroelectric material, the nanocomposite approach offers a platform to achieve multiferroic properties in 2D materials. Single-phase multiferroic materials are rarely reported because of the contradictory prerequisite for the coexistence of ferromagnetic and ferroelectric responses.[14] Recently, a series of Bi-based layered oxide materials such as $[Bi_3O_n][MO_2]_x$ (M = Al/Mn, BAMO), and $[Bi_nO_n][MO_2]_x$ (n = 2 or 3, M = Ni/Mn, BNMO), including $Bi_3Fe_2Mn_2O_x$ (BFMO322), have been discovered as a new class of room-temperature multiferroic materials using a pulsed laser deposition (PLD) technique.[15–19] These Bi-based layered supercell (LS) structures exhibit high T_c above room temperature.[18] Compared to their pseudocubic counterparts, these Bi-based LS structures share alternately layered stacks of Bi–O sublattices and M–O sublattices (M = Mn, Al, Ni, *etc.*).[15,16] Such LS structures with an Aurivillius and Ruddlesden–Popper phase present intriguing anisotropic physical properties, which allows diverse applications in superconductors, piezoelectric sensors, and photocatalysts.[20–22]

Moreover, these self-assembled LS structures offer great flexibility in structure construction and physical properties tailoring by varying the elemental molar ratio and/or by introducing buffer layers.[19,23–26] For example, the CeO_2 buffer layer is critical to the formation of the LS structure;[24] and certain elements (*e.g.* Mn, Al) can effectively tune the microstructure and the corresponding properties by varying their molar ratios.[25,26] However, most of these studies have focused on the supercell oxide thin films with the thickness in the range of 70–150 nm. Ultrathin layered oxides with a thickness around ~10 nm could result in novel physical properties, which have not yet been explored experimentally.

In this work, we conducted the thickness dependence study of ultrathin BFMO322 LS structure with a thickness range

[a]*School of Electrical and Computer Engineering, Purdue University, West Lafayette, IN 47907-2045, USA. E-mail: hwang00@purdue.edu*
[b]*School of Materials Engineering, Purdue University, West Lafayette, IN 47907-2045, USA*
[c]*Sandia National Laboratories, Albuquerque, NM, 87185, USA*

†Electronic supplementary information (ESI) available. See DOI: 10.1039/d1nr04975e

from 5 nm to 15 nm with the goal of achieving microstructure variation as well as tunable magnetic and optical properties. The schematic diagram (Fig. 1a) illustrates the stacking sequence of the BFMO322 LS, consisting of alternately stacked Bi–O layers and Mn/Fe–O layers. Unlike the weak magnetization in a pseudocubic Bi_2FeMnO_6 phase, the BFMO322 LS is expected to exhibit obvious ferromagnetic and ferroelectric responses due to its anisotropic layered lattice and the coupling between Mn and Fe cations. This thickness dependence study offers a simple approach for property tuning in 2D oxide materials with strong multiferroic properties for novel spintronic devices.

Experimental

Composite thin film deposition

The composite BFMO target was prepared by mixing Bi_2O_3, MnO_2, and Fe_2O_3 powders in stoichiometric ratio followed by solid-state sintering at 800 °C for 3 hours. The BFMO thin films were deposited on $LaAlO_3$ (LAO) (001) substrates using pulsed laser deposition (PLD, KrF excimer laser, λ = 248 nm). The substrate temperature was maintained at 600 °C, while an optimized oxygen pressure of 200 mTorr and a laser frequency of 2 Hz were maintained during the thin film deposition. The deposition time was varied from 1 to 4 minutes to vary the thickness of the films. All films were then cooled down to room temperature at 10 °C min^{-1} under a 500 Torr oxygen ambient pressure.

Microstructural characterization

The crystallinity and microstructures of the as-deposited BFMO films were characterized by X-ray diffraction (XRD, PANalytical Empyrean, Cu K_α radiation), high-angle annular dark field scanning transmission electron microscopy (HAADF-STEM), energy-dispersive X-ray spectroscopy (EDS) (Thermo Fisher Scientific TALOS F200× operated at 200 kV), and high-resolution HAADF-STEM (aberration–corrected Thermo Fisher Scientific Titan G2 – operated at 200 kV). Cross-sectional TEM samples were prepared using the standard manual grinding procedure, followed by dimpling and ion milling (Gatan Inc. PIPS 695 precision ion polishing system).

Magnetic and optical properties characterization

The magnetic properties of the BFMO films were measured in a magnetic property measurement system (MPMS, Quantum Design MPMS-3). The magnetic field was applied in both parallel and perpendicular directions to determine the in-plane

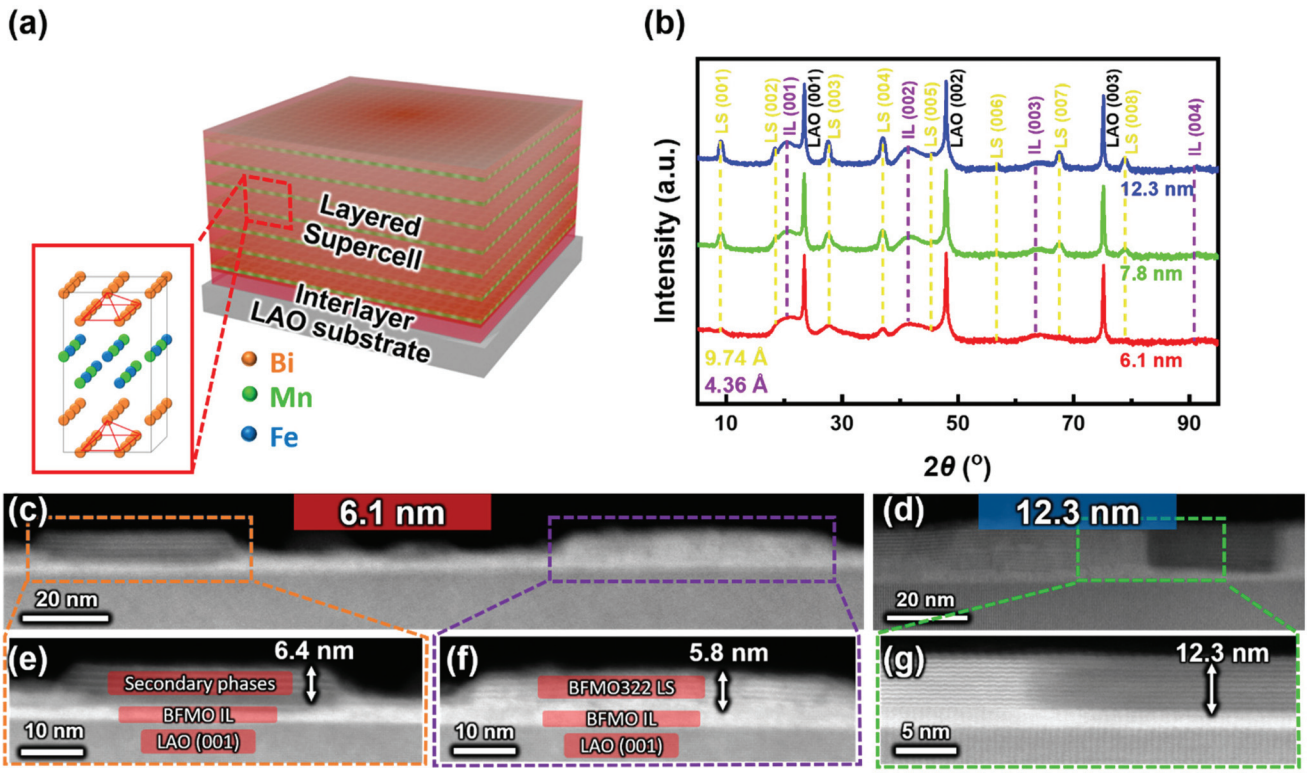

Fig. 1 Microstructural characterization. (a) Schematic diagram of the $Bi_3Fe_2Mn_2O_{10+\delta}$ layered supercell (BFMO322 LS) structure and the BFMO interlayer on the LAO substrate. The enlarged schematic illustrates atomic modeling of the BFMO322 cation sublattice. (b) XRD θ–2θ scans of BFMO films at three thicknesses showing two sets of (00l) peaks with different lattice constants, corresponding to the BFMO322 LS (yellow dashed line) and the BFMO interlayer (IL) with pseudo-perovskite structure (purple dashed line), respectively. (c and d) Cross-sectional low-magnification HAADF-STEM images of the 6.1 nm and 12.3 nm BFMO films, respectively. (e–g) HAADF-STEM images of the marked region in (c and d), illustrating the morphology of films with different thicknesses.

(IP) and out-of-plane (OP) magnetic behavior of the BFMO films, respectively. The film signal was calculated by a point-by-point subtraction of the $Moment_{sample+background}$ and $Moment_{background}$ measurement. The piezoelectric response of the BFMO films were investigated in a piezoresponse force microscopy (PFM, Bruker Dimension Icon) using a conductive Pt–Ir coated Si tip (SCM-PIT). CeO_2 buffer layer was deposited as the bottom electrode before the measurement.

The optical dielectric permittivity of the BFMO films were collected and analyzed using a spectroscopic ellipsometry (J.A. Woollam RC2). The ellipsometer parameters psi (ψ) and delta (Δ) were obtained with a spectrum range of 500–2500 nm at three angles of incidence (55°, 65°, 75°). The dielectric permittivity was then obtained by fitting ψ and Δ in CompleteEASE software with appropriate GenOsc models. All the samples were fitted in an anisotropic manner due to the supercell structure of the films. The normal incident depolarized transmittance (T%) of the BFMO films were collected in a UV-Vis-NIR spectrophotometer (PerkinElmer Lambda 1050) with the baseline correction. The direct band gaps were extrapolated using the Tauc-plot method.

Results and discussion

The crystallinity and microstructure of the as-deposited ultrathin BFMO films were first characterized using X-ray diffraction (XRD). Fig. 1b compares the XRD θ–2θ scans of the BFMO films on LAO (001) substrates with different film thicknesses. All three samples present two sets of distinct (00l) diffraction peaks, indicating the highly textured growth of BFMO films along the out-of-plane (OP) direction. The peaks marked as LS (00l) represent the layered supercell structure with an out-of-plane d-spacing of 9.74 Å, which consists of Bi–O and Mn–Fe–O layers. On the other hand, the peaks marked as IL (00l) represent the interlayer with an out-of-plane d-spacing of 4.36 Å, which has a pseudo-perovskite structure between the LS structure and the LAO substrate. It is noted that the XRD results present similar diffraction patterns for samples with different thicknesses, and no obvious peak shift was observed. The result suggests there is a similar crystal structure and crystalline quality of all the BFMO films.

The microstructure and composition of BFMO films with different thicknesses were investigated using selected area electron diffraction (SAED), high-angle annular dark field scanning transmission electron microscopy (HAADF-STEM), and energy-dispersive X-ray spectroscopy (EDS). The cross-sectional STEM images in Fig. 1c and d clearly demonstrate the microstructure evolution for ultrathin BFMO films. A thin IL up to 4 nm was observed in all three samples, consistent with XRD observation in Fig. 1b. The presence of the IL is to relieve the mismatch strain between the BFMO322 LS structure and the LAO substrate. As the biaxial strain accumulates through the IL, asymmetric strain relaxation occurs due to unit cell anisotropy (c/a = 1.15), which leads to the interface reconstruction and consequently triggers the misfit layered bismuth compound stacking.[15,16] Above the critical thickness, the films exhibit a clear layered stacking growth of BFMO322 LS as a result of interface reconstruction. According to prior work, the IL resembles the pseudo-perovskite structure and the LS has a cation ratio of Bi : Fe : Mn = 3 : 2 : 2 (*i.e.*, $Bi_3Fe_2Mn_2O_{10+\delta}$, BFMO322).[15,16] Specifically, the dependence of formation energy on oxygen vacancies was calculated using DFT theory,[16] and the stoichiometric ratio for the LS phase was determined as $Bi_6Fe_4Mn_4O_{21}$. In this work, the 6.1 nm thick sample (Fig. 1e and f) presents a discontinuous ultrathin film (*i.e.*, an island growth of BFMO322 LS structure). In addition, a minor secondary phase (Fig. 1e) was formed, and this phase was identified as a $MnFe_2O_x$ phase by EDS analysis (Fig. S1†). The observed structure is in accordance with two sets of dominant (00l) peaks in the XRD pattern (Fig. 1b). The XRD peak intensity of BFMO322 LS in 6.1 nm thick film is relatively low since BFMO322 LS is of similar thickness as the IL. On the contrary, the 12.3 nm thick sample (Fig. 1d and g) presents a continuous film, and the thicker BFMO322 LS structure gave rise to more intense LS peaks in the XRD pattern. The presence of secondary phase peaks in the XRD pattern was not detected due to small volume percentage of the phase in the whole film.

Atomic-scale HAADF-STEM images were taken from the LAO [100] zone axis for further interfacial investigation, as demonstrated in Fig. 2. An approximately 4 nm-thick pseudo-perovskite IL was formed between the BFMO322 LS structure and the LAO substrate, which served as a strain relaxation template to induce the layered stacking in the LS structure. The BFMO322 LS structure in this work is composed of alternately aligned Bi_2O_2 slabs (orange layers in Fig. 2a) and distorted MnO_6/FeO_6 octahedra (green and blue layers in Fig. 2a), which is consistent with prior reports.[15,17] Interestingly, misfit dislocations (denoted as red arrows) are distributed along the heterointerface with the average spacing approximately 6 nm. As a consequence of asymmetric lattice distortion along the [100] axis, these misfit dislocations were generated to further accommodate the strain between the BFMO322 LS structure and the IL. In addition, distinct diffraction dots in the corresponding SAED pattern (shown as an inset in Fig. 2a) confirm the high-quality epitaxial growth of the ultrathin BFMO322 LS structure along the OP direction despite being ultrathin films. Fig. 2b was used to investigate the atomic arrangement and to measure the lattice parameters of the BFMO322 LS and the IL. Since the intensity in HAADF-STEM is proportional to the atomic number Z^2, the bright contrast layers in Fig. 2b represent the Bi–O slabs (Z_{Bi} = 83), and the dark contrast layers represent the Mn/Fe–O octahedra (Z_{Mn} = 25 and Z_{Fe} = 26). An atomic model was demonstrated as an inset to compare the stacking arrangement in the BFMO322 LS structure and the IL. In the BFMO322 LS structure, both Bi_2O_2 and MnO_6/FeO_6 layers were stacked in a highly epitaxial yet zigzag manner, and the adjacent Bi_2O_2 layers share the periodic cation position along the OP direction (shown as red triangles in Fig. 2b). In contrast, Bi_2O_2 and MnO_6/FeO_6 layers within the IL exhibit a typical pseudo-perovskite lattice, in which Mn/Fe atoms sit in

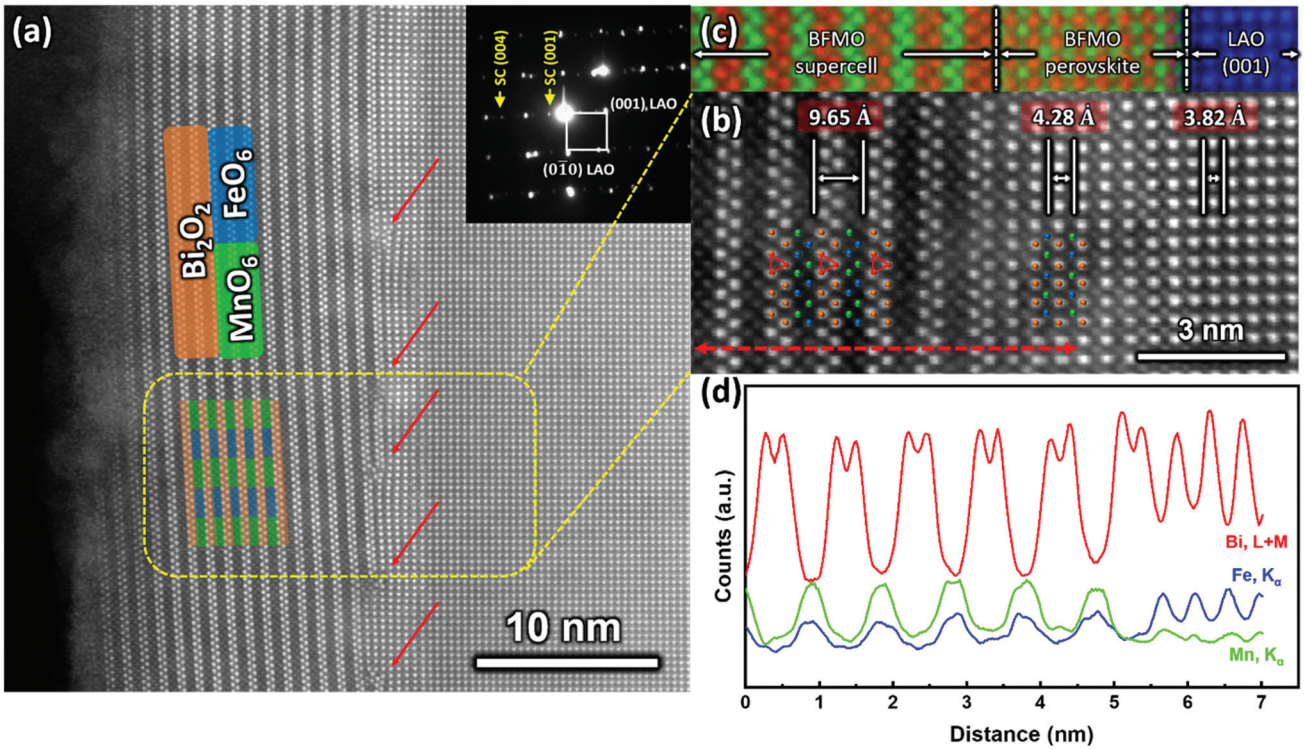

Fig. 2 Atomic-scale microstructural characterization. (a) Cross-sectional HR-STEM image of 12.3 nm BFMO film along the LAO [100] zone axis. Misfit dislocations are denoted as red arrows, with the average spacing around 6 nm. The inset presents the SAED pattern. (b) HR-STEM image of the marked region in (a), along with the atomic models of the BFMO322 LS and BFMO pseudo-perovskite IL cation sublattices. (c) Corresponding atomic-scale EDS color map of the interface region in (b), indicating the atom distribution in BFMO322 LS, BFMO IL and LAO substrate, respectively. (d) Line profiles for Bi (red), Mn (green), and Fe (blue) atoms along the red dashed arrow in (b).

the centers of Bi square lattices. The out-of-plane *d*-spacings of the BFMO322 LS structure and the IL were estimated to be 9.65 Å and 4.28 Å, respectively, suggesting a smaller lattice misfit strain between the IL and the LAO substrate. The estimated periodicity is consistent with the above XRD analysis. The atomic-scale EDS color maps in Fig. 2c and the EDS line profiles in Fig. 2d indicate the Bi (L + M, red), Mn (Kα, green), and Fe (Kα, blue) distribution along the red dashed arrow in Fig. 2b. The structure of BFMO322 LS has also been verified by atomic-scale EDS mapping (Fig. S2†). The results clearly distinguish two different structures existed in the ultrathin film: (1) the BFMO322 LS structure consisting of the distinctive bilayer stacking of Bi_2O_2 slabs and distorted MnO_6/FeO_6 octahedra and (2) the pseudo-perovskite IL consisting of single layer stacking of Bi_2O_2 and MnO_6/FeO_6 layers. Mn and Fe atoms occupy equivalent positions within the MnO_6/FeO_6 octahedra in both the IL and the BFMO322 LS structure, while the atomic ratios may vary.

Based on the above observation, the ultrathin BFMO322 LS structure likely originates from the Aurivillius phases. In an Aurivillius lattice, Bi_2O_2 layers are stacked alternately with $A_{n-1}B_nO_{3n+1}$ perovskite layers, which generates a unique layered structure with great structural flexibility.[27,28] According to the Matthews–Blakeslee model, the substrate-induced biaxial strain could also contribute to the formation of LS structure.[29] The asymmetric lattice distortion causes the interfacial reconstruction accompanied by misfit defects. The concomitant strain relaxation at the reconstructed interface then triggers the layered stacking of ultrathin BFMO322 LS films.[17,24] Based upon the theoretical estimation using the Pertsev model, misfit strain promotes the growth of epitaxially constrained films that are not possible in equilibrium single crystals.[30,31] It is noted that the secondary phases in ultrathin BFMO films is also likely attributed to the biaxial strain. The strain induced crystal distortion will modify the Mn/Fe–O bond angles and length. These structural modifications promote the secondary phases and cause changes in physical properties. Similar secondary phases within the films have been observed previously in GeSn/Ge and LCMO/STO ultrathin heterostructures.[32,33]

The multiferroic response of the ultrathin BFMO films was investigated using both magnetic property measurement system (MPMS) and piezoresponse force microscopy (PFM), as illustrated in Fig. 3. Initially, the room-temperature magnetic hysteresis (*M*–*H*) loops for three BFMO films were compared in Fig. 3a and b. The magnetic field was applied in both parallel and perpendicular directions to determine the in-plane (IP) and out-of-plane (OP) magnetic behavior. Overall, all the ultrathin BFMO films exhibit apparent magnetic behavior in both IP and OP directions. The corresponding saturation magneti-

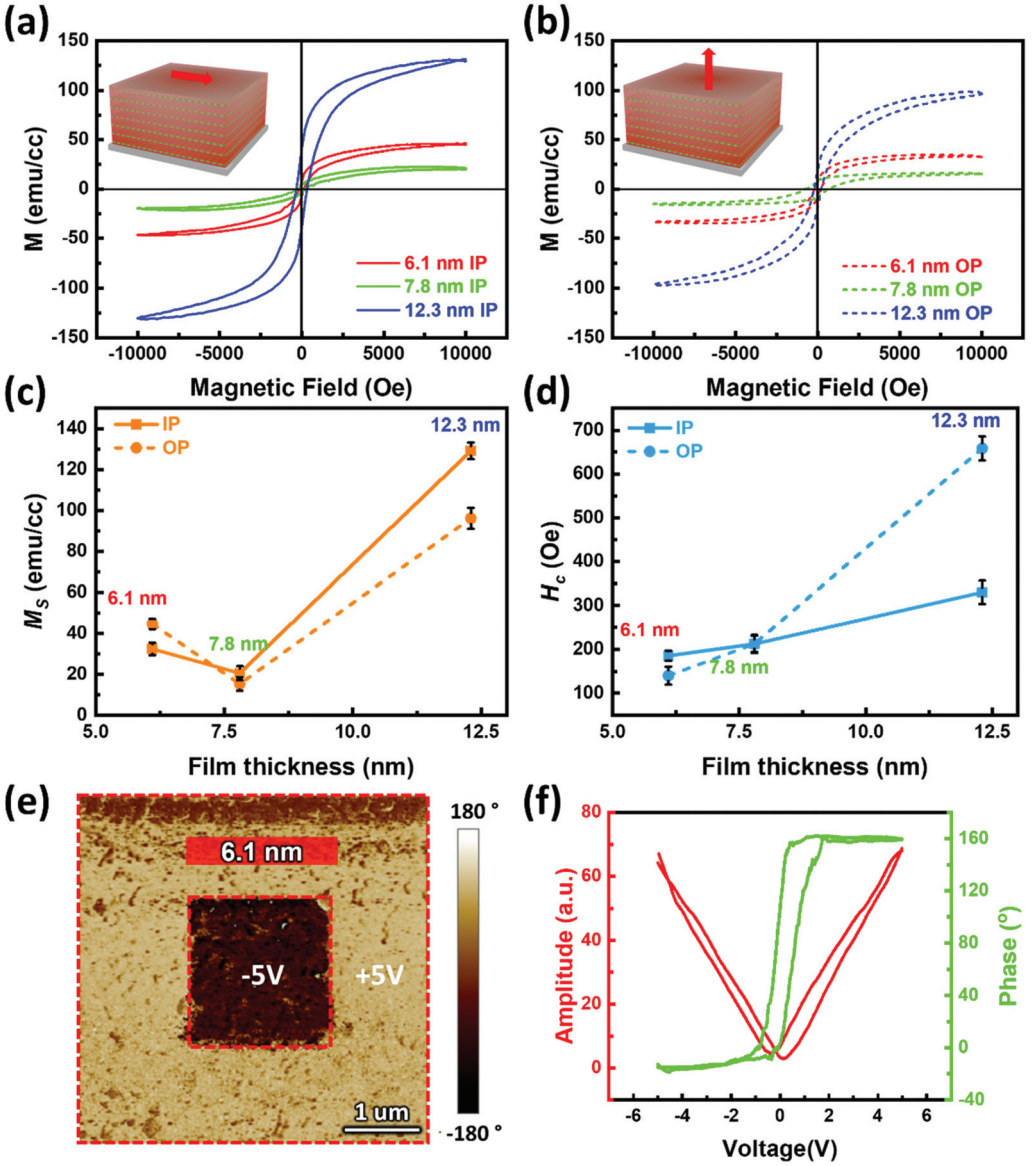

Fig. 3 Multiferroic properties. (a) In-plane (IP) and (b) out-of-plane (OP) magnetic hysteresis loop (M–H) of BFMO films with different thickness measured at 300 K. (c) saturation magnetization (M_s) and (d) coercivity (H_c) in both IP and OP directions as a function of the film thickness. (e) PFM vertical phase map of 6.1 nm BFMO film after +5 V writing over a 5 × 5 μm^2 square box followed by −5 V rewriting over a 2 × 2 μm^2 central square box. (f) The amplitude (red) and phase (green) switching curves of 6.1 nm BFMO film as a function of bias voltage.

zation (M_s, emu cm^{-3}) and coercive field (H_c, Oe) are plotted in Fig. 3c and d to study the magnetic anisotropy in ultrathin BFMO films. It is noted that the 12.3 nm thick film achieved a robust saturation magnetization of 129 and 96 emu cm^{-3} in the IP and OP directions, respectively, which is significantly higher than other 2D materials candidates.[34,35] The room-temperature saturation magnetization for 12.3 nm thick film is comparable to the value of 40–60 nm BFMO LS films on either LAO substrates or CeO_2 buffered STO substrates from previous reports.[15,16,24,25] In addition, the anisotropic magnetic response in all samples switches from OP dominating (6.1 nm) to IP dominating (12.3 nm) as the film thickness increases. In other words, the magnetic easy axis was changed from OP to IP. The 7.8 nm film did not show a clear magnetic anisotropy and had a relatively low saturation magnetization, suggesting a comparable OP and IP magnetic response. Unlike the weak ferromagnetism in the tetragonal Bi_2FeMnO_6 films,[36] the strong ferromagnetism in ultrathin BFMO322 LS structure is attributed to the coupled Mn/Fe cations. To be specific, the zigzag arrangement of Mn and Fe cations promotes the Mn–O–Fe orbital hybridization and facilitates the double exchange between mixed-valence cations.[37,38] Therefore, such atomic arrangement gives rise to the magnetic coupling in the LS structure, and the consequent spin–orbit interaction causes the magnetic anisotropy.

The ferroelectric properties of the ultrathin BFMO films were explored using PFM, as illustrated in Fig. 3e and f. CeO_2

buffer layers were deposited as the bottom electrode for the ferroelectric measurement. Initially, the distinct image contrast in Fig. 3e demonstrates the OP phase switching behavior after the writing/rewriting process, where a +5 V tip bias was first applied on 5 × 5 μm^2 square box followed by a −5 V tip bias applied on its central area. The OP phase (green) and amplitude (red) switching curves in Fig. 3f also demonstrate the ferroelectric switching of ultrathin BFMO films. When the bias direction is switched, a symmetric change in the amplitude and a characteristic hysteresis loop with 180° phase switching were observed. As a result, the room-temperature phase switching behavior elucidates the switchable and ferroelectric nature in ultrathin BFMO films. Additionally, the ferroelectric response is comparable regardless of the thickness variation (Fig. S3†). The comparable ferroelectric properties are attributed to the similar layer-by-layer stacking structure in all samples, where the ferroelectricity in ultrathin BFMO films possibly originates from the displacement of lone–pair electrons and the resulted non-centrosymmetric lattice structure.[18,39] Specifically, the strong electrostatic repulsion caused by the covalent bonding between Bi^{3+} and O^{2-} shifts the $6s^2$ lone pair in Bi cations; the displacement thus distorts the unit cell and breaks the spatial symmetry within the lattice. Overall, the coexistence of ferromagnetism and ferroelectricity indicates the multiferroic nature in the ultrathin BFMO films at room temperature.

A tunable optical response, including dielectric permittivity and optical bandgap, are demonstrated in Fig. 4 and S4.† Because of the anisotropic nature of the LS structure, the dielectric permittivity was modeled with uniaxial anisotropy. Tauc–Lorentz oscillator models, which enforce the Kramers–Kronig consistency, were used to fit the IP ($\varepsilon_{\parallel}$) and OP ($\varepsilon_{\perp}$) permittivity. The real and imaginary parts of dielectric permittivity were compared at different thickness values in Fig. 4 and Fig. S5,† respectively. As the thickness increases, the anisotropy of the ultrathin BFMO films switches from OP dominating (Fig. 4a) to IP dominating (Fig. 4c). The result is consistent with the anisotropy observed in the magnetic property dis-

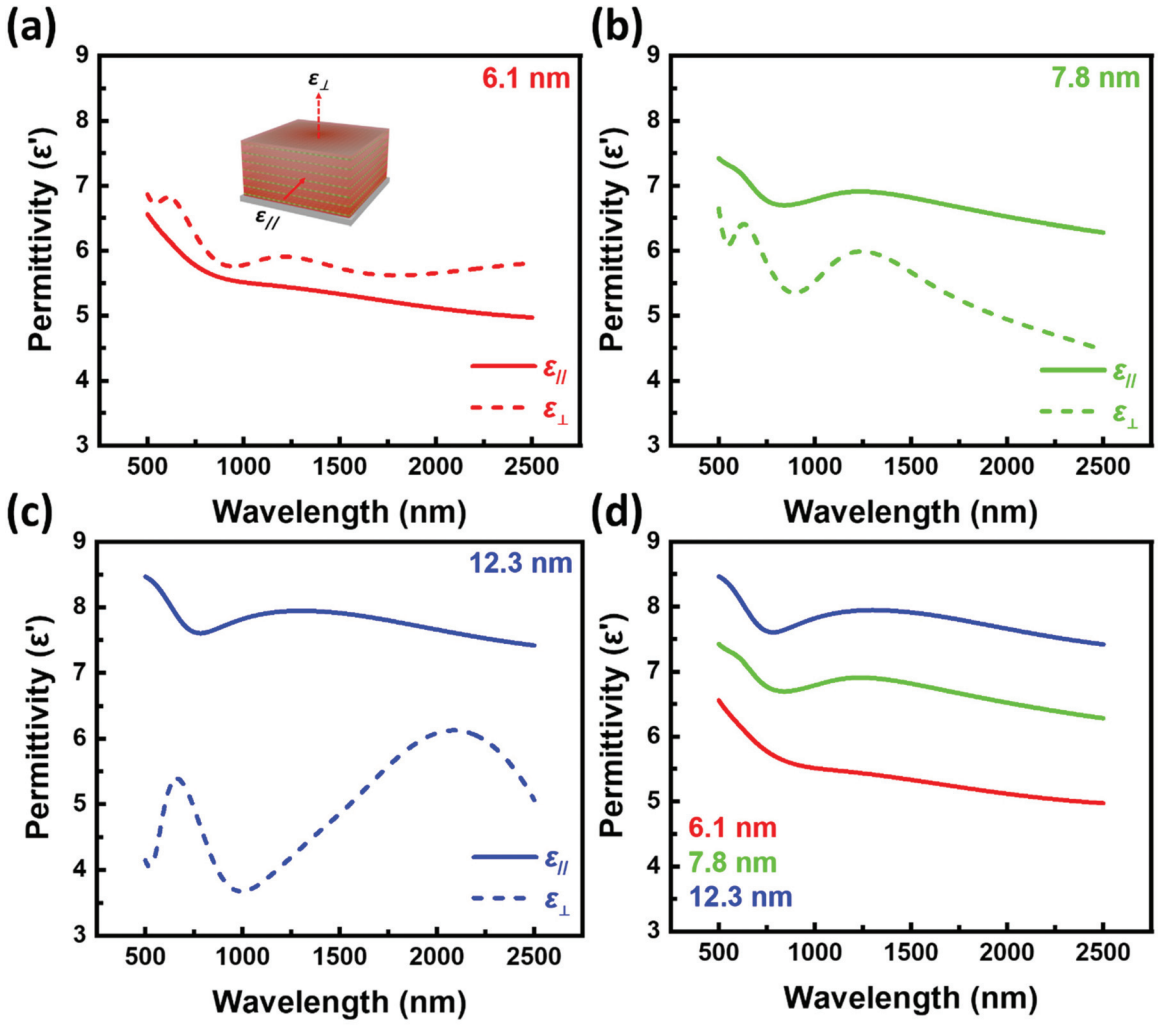

Fig. 4 Tunable dielectric properties. (a–c) Real part of the permittivity of BFMO films with different thickness in both IP ($\varepsilon_{\parallel}$, solid line) and OP ($\varepsilon_{\perp}$, dashed line) directions. (d) Comparison of the IP permittivity of BFMO films with different thickness.

cussed above. Interestingly, the IP permittivity of three samples possesses a comparable trend and can be systemically tuned by varying the thickness and the film morphology, as compared in Fig. 4d. The LS structure gives rise to the similar IP permittivity since it plays a vital role in the light-matter interactions. The surface morphology is also a more dominant factor for thinner samples as reported previously.[40,41] In addition, Fig. S4† illustrates the UV-vis-NIR transmittance spectra for all three films. The Tauc-plot method was employed to calculate the corresponding direct band gaps. Detailed band gap calculation confirms the band gap can be tuned from 2.63 eV to 2.47 eV as a function of film thickness. The band gaps reported here are slightly higher than the theoretical values from DFT calculations,[25] possibly due to the presence of the secondary phases and the one-dimensional quantum confinement effect for ultrathin films.[42] Overall, the optical properties of ultrathin BFMO films can be systematically tuned by varying thickness and surface morphology.

This thickness dependence study of ultrathin BFMO films provides insight into the microstructure evolution for Bi-based LS structures. It also helps develop an understanding of the initial nucleation and growth mechanism of the oxide LS structure and explore other layered oxide systems for electronic and magnetic applications. Compared to other 2D materials lacking a robust intrinsic ferromagnetic response, such as feroxyhyte nanosheets and MnGa films,[35,43] the ultrathin BFMO322 LS structures exhibit a strong room-temperature multiferroic response including high saturation magnetization and low coercivity. On the other hand, highly anisotropic behavior is also realized in these Bi-based LS structures; and the tunable magnetic and optical properties in both IP and OP directions have potential applications in data storage and on-chip sensors. The novelty of this work lies in the Bi-based LS structures demonstrating great flexibility in tailoring the materials properties and achieving strong anisotropic multiferroics in 2D structures. Other ultra-thin LS candidates, such as Bi_2AlMnO_6, Bi_2CoMnO_6, and Bi_2NiMnO_6 can also be explored as atomic thin 2D layered oxides for applications as integrated electronic and magnetic devices.

Conclusions

In summary, ultrathin BFMO layered oxide films (from 6.1 nm to 12.3 nm) have been grown on LAO (001) substrates epitaxially with a thin pseudo-perovskite IL to release biaxial strain. The epitaxial BFMO322 LS structure is self-assembled with minor secondary phases. Specifically, the BFMO322 LS structure consists of two mismatch-layered sublattices: alternately layered stacks of two-layer-thick Bi–O slabs and two-layer-thick Mn/Fe–O octahedra slabs. The physical properties, including ferromagnetic and ferroelectric properties, dielectric permittivity, and optical bandgap can be effectively tuned by thickness variation. A robust saturation magnetization value of 129 and 96 emu cm^{-3} is achieved in 12.3 nm thick film in the IP and OP directions, respectively. In addition, the anisotropy of all ultrathin BFMO films switches from OP dominating to IP dominating as the thickness increases. These tuning effects are attributed to the zigzag arrangement of Mn/Fe cations and non-centrosymmetric nature of the structure. This study demonstrates a new 2D material candidate with tunable multifunctionalities for novel spintronic devices.

Conflicts of interest

There are no conflicts to declare.

Acknowledgements

The authors acknowledge the support from the Office of Naval Research for the thin film growth effort (N00014-1-20-2600). Z. H. and H. W. acknowledge the support from the U.S. National Science Foundation (DMR-1809520 and DMR-2016453) for structural and property characterizations and high-resolution STEM/EDS analysis. D. Z. and H. W. acknowledge the support from the Office of Naval Research under contract no. N00014-17-1-2087 and N00014-20-1-2043 for the TEM/STEM effort. Sandia National Laboratories is a multi-program laboratory managed and operated by National Technology and Engineering Solutions of Sandia, LLC., a wholly owned subsidiary of Honeywell International, Inc., for the U.S. Department of Energy's National Nuclear Security Administration under contract DE-NA0003525. This paper describes objective technical results and analysis. Any subjective views or opinions that might be expressed in the paper do not necessarily represent the views of the U.S. Department of Energy or the United States Government.

References

1 A. K. Geim and K. S. Novoselov, *Nat. Mater.*, 2007, **6**, 183.
2 J. Zhou, Q. Wang, Q. Sun, X. S. Chen, Y. Kawazoe and P. Jena, *Nano Lett.*, 2009, **9**, 3867.
3 S. Manzeli, D. Ovchinnikov, D. Pasquier, O. V. Yazyev and A. Kis, *Nat. Rev. Mater.*, 2017, **2**, 1.
4 X. Qian, J. Liu, L. Fu and J. Li, *Science*, 2014, **346**, 1344.
5 Y. Chen, Y. Sun, J. Peng, J. Tang, K. Zheng and Z. Liang, *Adv. Mater.*, 2018, **30**, 1703487.
6 P. Chen, Y. Bai, S. Wang, M. Lyu, J.-H. Yun and L. Wang, *Adv. Funct. Mater.*, 2018, **28**, 1706923.
7 J. Zhou and Q. Sun, *J. Am. Chem. Soc.*, 2011, **133**, 15113.
8 M. Zhao, Y. Wang, Q. Ma, Y. Huang, X. Zhang, J. Ping, Z. Zhang, Q. Lu, Y. Yu, H. Xu, Y. Zhao and H. Zhang, *Adv. Mater.*, 2015, **27**, 7372.
9 S. Roche, J. Åkerman, B. Beschoten, J. C. Charlier, M. Chshiev, S. P. Dash, B. Dlubak, J. Fabian, A. Fert, M. Guimarães, F. Guinea, I. Grigorieva, C. Schönenberger, P. Seneor, C. Stampfer, S. O. Valenzuela, X. Waintal and B. Van Wees, *2D Mater.*, 2015, **2**, 030202.
10 K. F. Mak and J. Shan, *Nat. Photonics*, 2016, **10**, 216.

11 Q. H. Wang, K. Kalantar-Zadeh, A. Kis, J. N. Coleman and M. S. Strano, *Nat. Nanotechnol.*, 2012, **7**, 699.
12 M. Gibertini, M. Koperski, A. F. Morpurgo and K. S. Novoselov, *Nat. Nanotechnol.*, 2019, **14**, 408.
13 J. Rybczynski, U. Ebels and M. Giersig, *Colloids Surf., A*, 2003, **219**, 1.
14 N. A. Hill, *J. Phys. Chem. B*, 2000, **104**, 6694.
15 A. Chen, H. Zhou, Z. Bi, Y. Zhu, Z. Luo, A. Bayraktaroglu, J. Phillips, E. M. Choi, J. L. MacManus-Driscoll, S. J. Pennycook, J. Narayan, Q. Jia, X. Zhang and H. Wang, *Adv. Mater.*, 2013, **25**, 1028.
16 W. Zhang, M. Li, A. Chen, L. Li, Y. Zhu, Z. Xia, P. Lu, P. Boullay, L. Wu, Y. Zhu, J. L. MacManus-Driscoll, Q. Jia, H. Zhou, J. Narayan, X. Zhang and H. Wang, *ACS Appl. Mater. Interfaces*, 2016, **8**, 16845.
17 Y. Zhu, A. Chen, H. Zhou, W. Zhang, J. Narayan, J. L. Macmanus-Driscoll, Q. Jia and H. Wang, *APL Mater.*, 2013, **1**, 050702.
18 L. Li, P. Boullay, P. Lu, X. Wang, J. Jian, J. Huang, X. Gao, S. Misra, W. Zhang, O. Perez, G. Steciuk, A. Chen, X. Zhang and H. Wang, *Nano Lett.*, 2017, **17**, 6575.
19 L. Li, P. Boullay, J. Cheng, P. Lu, X. Wang, G. Steciuk, J. Huang, J. Jian, X. Gao, B. Zhang, S. Misra, X. Zhang, K. Yang and H. Wang, *Mater. Today Nano*, 2019, **6**, 100037.
20 M. K. Wu, J. R. Ashburn, C. J. Torng, P. H. Hor, R. L. Meng, L. Gao, Z. J. Huang, Y. Q. Wang and C. W. Chu, *Phys. Rev. Lett.*, 1987, **58**, 908.
21 H. Du and X. Shi, *J. Phys. Chem. Solids*, 2011, **72**, 1279.
22 S. Ida and T. Ishihara, *J. Phys. Chem. Lett.*, 2014, **5**, 2533.
23 X. Gao, L. Li, D. Zhang, X. Wang, J. Jian, Z. He and H. Wang, *Nanoscale*, 2020, **12**, 5914.
24 L. Li, W. Zhang, F. Khatkhatay, J. Jian, M. Fan, Q. Su, Y. Zhu, A. Chen, P. Lu, X. Zhang and H. Wang, *ACS Appl. Mater. Interfaces*, 2015, **7**, 11631.
25 L. Li, J. Cheng, H. Wang, J. Huang, X. Gao, X. Wang, S. Misra, B. Zhang, J. Jian, A. Chen, P. Lu, X. Qian, K. Yang and H. Wang, *Cryst. Growth Des.*, 2019, **19**, 7088.
26 S. Misra, L. Li, X. Gao, J. Jian, Z. Qi, D. Zemlyanov and H. Wang, *Nanoscale Adv.*, 2020, **2**, 315.
27 K. R. Kendall, C. Navas, J. K. Thomas and H. C. Zur Loye, *Chem. Mater.*, 1996, **8**, 642.
28 R. E. Schaak and T. E. Mallouk, *Chem. Mater.*, 2002, **14**, 1455.
29 J. W. Matthews, D. C. Jackson and A. Chambers, *Thin Solid Films*, 1975, **26**, 129.
30 Z. G. Ban and S. P. Alpay, in *Mater. Res. Soc. Symp. - Proc.*, Materials Research Society, 2002, pp. 233–238.
31 N. A. Pertsev, A. G. Zembilgotov and A. K. Tagantsev, *Phys. Rev. Lett.*, 1998, **80**, 1988.
32 S. Estradé, J. M. Rebled, J. Arbiol, F. Peiró, I. C. Infante, G. Herranz, F. Sánchez, J. Fontcuberta, R. Córdoba, B. G. Mendis and A. L. Bleloch, *Appl. Phys. Lett.*, 2009, **95**, 072507.
33 H. Li, Y. X. Cui, K. Y. Wu, W. K. Tseng, H. H. Cheng and H. Chen, *Appl. Phys. Lett.*, 2013, **102**, 251907.
34 A. Y. S. Eng, H. L. Poh, F. Šaněk, M. Maryško, S. Matějková, Z. Sofer and M. Pumera, *ACS Nano*, 2013, **7**, 5930.
35 P. Chen, K. Xu, X. Li, Y. Guo, D. Zhou, J. Zhao, X. Wu, C. Wu and Y. Xie, *Chem. Sci.*, 2014, **5**, 2251.
36 E. M. Choi, S. Patnaik, E. Weal, S. L. Sahonta, H. Wang, Z. Bi, J. Xiong, M. G. Blamire, Q. X. Jia and J. L. MacManus-Driscoll, *Appl. Phys. Lett.*, 2011, **98**, 012509.
37 L. Bi, A. R. Taussig, H.-S. Kim, L. Wang, G. F. Dionne, D. Bono, K. Persson, G. Ceder and C. A. Ross, *Phys. Rev. B: Condens. Matter Mater. Phys.*, 2008, **78**, 104106.
38 I. V. Solovyev, *J. Phys.: Condens. Matter*, 2008, **20**, 33.
39 R. Seshadri and N. A. Hill, *Chem. Mater.*, 2001, **13**, 2892.
40 P.-T. Shen, Y. Sivan, C.-W. Lin, H.-L. Liu, C.-W. Chang and S.-W. Chu, *Opt. Express*, 2016, **24**, 19254.
41 C. B. Parker, J. P. Maria and A. I. Kingon, *Appl. Phys. Lett.*, 2002, **81**, 340.
42 E. S. M. Goh, T. P. Chen, C. Q. Sun and Y. C. Liu, *J. Appl. Phys.*, 2010, **107**, 24305.
43 M. Tanaka, J. P. Harbison, J. Deboeck, T. Sands, B. Philips, T. L. Cheeks and V. G. Keramidas, *Appl. Phys. Lett.*, 1993, **62**, 1565.